Catalysis Science & Technology

PAPER

View Article Online
View Journal | View Issue

Cite this: *Catal. Sci. Technol.*, 2018, **8**, 3144

Tuning nanosheet Fe_2O_3 photoanodes with C_3N_4 and p-type CoO_x decoration for efficient and stable water splitting†

Zongwei Mei,[a] Yehuan Li,[a] Xiaoyang Yang,[a] Wenju Ren,[a] Shengfu Tong,[b] Ning Zhang,[c] Wenguang Zhao,[a] Yuan Lin[d] and Feng Pan*[a]

Received 12th April 2018,
Accepted 22nd May 2018

DOI: 10.1039/c8cy00729b

rsc.li/catalysis

Fe_2O_3 photoanodes are ideal candidates for photoelectrochemical (PEC) water splitting. However, the charge recombination in the bulk and at the photoanode/electrolyte interface decreases their PEC performance. Here, C_3N_4 and p-type CoO_x are firstly decorated on Fe_2O_3 nanosheets for PEC performance enhancement and mechanism study. The photocurrent densities of Fe_2O_3/C_3N_4 and $Fe_2O_3/C_3N_4/CoO_x$ photoanodes are about 1.6 and 2 times at 1.23 V *vs.* RHE (reversible hydrogen electrode) compared with that of the Fe_2O_3 film (0.74 mA cm^{-2}) under simulated sun light irradiation. Correspondingly, their photocurrent onset potentials are negatively shifted by about 0.09 and 0.19 V compared with that of Fe_2O_3 (0.81 V_{RHE}). The solar-to-hydrogen conversion efficiency reaches 0.17% and the incident photo-to-current conversion efficiency (IPCE) achieves 81.7% at 385 nm for the $Fe_2O_3/C_3N_4/CoO_x$ hybrid photoanode. The matched band alignments between Fe_2O_3 and C_3N_4 result in more efficient charge separation, and the p-type CoO_x cocatalyst reduces surface recombination and shows quicker water oxidation reaction kinetics at the semiconductor/electrolyte interface.

Introduction

Photoelectrochemical transformation of water into clean H_2 energy is attracting increasing research interest due to the desire of decreasing the use of fossil fuels and the accompanying environmental issues. Fe_2O_3 photoanodes are ideal candidates for PEC water oxidation due to their appropriate band gap (~2 eV), high stability, and rich abundance.[1] However, the PEC performance is limited by their poor conductivity, short hole diffusion length, and sluggish water oxidation kinetics at the semiconductor/electrolyte interface,[2] which result in low photocurrent density and large overpotential for water oxidation.

Many efforts have been dedicated to enhance PEC activities of Fe_2O_3 photoanodes. Element doping is an efficient way to improve the conductivity of Fe_2O_3 photoanodes, including Sn^{4+},[3–5] Ti^{4+},[6,7] Ta^{5+},[8] Ge^{4+},[9] Mn^{2+},[10] Pt^{4+},[11,12] Si^{4+},[13] P^{5+},[14] Zr^{4+},[15] *etc.* For the improvement of separation and migration ability of photoexcited e^-/h^+ pairs, coupling other semiconductors with Fe_2O_3 has been densely studied, such as Fe_2O_3/Fe_2TiO_5,[16–18] Fe_2O_3/WO_3,[19] $Fe_2O_3/ZnFe_2O_4$,[20] $Fe_2O_3/CaFe_2O_4$,[21] and Co-doped $Fe_2O_3/MgFe_2O_4$.[22] Polymeric C_3N_4 is a visible-light-sensitive semiconductor with good thermal and chemical stability for photocatalytic H_2 and/or O_2 evolution from water.[23–25] It has also been used as an efficient composite layer for PEC water oxidation, which can greatly enhance the PEC performances. Zhang *et al.* modified Fe_2O_3 and Ti-doped Fe_2O_3 with C_3N_4 by chemical vapor deposition or a dip-coating approach.[26,27] Zhu *et al.* fabricated a unique 3D heterojunction of a C_3N_4/Ba-doped TaON photoanode,[28] Feng and Guo groups synthesized a C_3N_4/WO_3 composite for PEC water splitting,[29,30] and Bi *et al.* demonstrated a $C_3N_4/BiVO_4$ photoanode.[31] Furthermore, p-type CoO_x decoration could facilitate charge transfer and it could act as a cocatalyst to modify the surface reaction kinetics of a photoanode.[32–34] Based on the above reports, it is desired that the $Fe_2O_3/C_3N_4/CoO_x$ hybrid photoanode would show good PEC performance for water oxidation.

Usually, fluorine-doped tin oxide (FTO) is used as a conductive substrate of Fe_2O_3 photoanodes, and high temperature annealing is necessary to enhance the PEC performance *via* Sn^{4+} diffusion into Fe_2O_3.[5] However, the morphology size of Fe_2O_3 becomes larger after the heat treatment,[3] which is not beneficial to maximize the PEC performance of Fe_2O_3

[a] *School of Advanced Materials, Peking University Shenzhen Graduate School, Shenzhen 518055, China. E-mail: panfeng@pkusz.edu.cn; Tel: +86 755 26033200*
[b] *MOE Key Laboratory of Bioinorganic and Synthetic Chemistry, School of Chemistry, Sun Yat-Sen University, Guangzhou 510275, China*
[c] *Department of Materials Chemistry, School of Materials Science and Engineering, Central South University, Hunan 410083, China*
[d] *Key Laboratory of Photochemistry, Institute of Chemistry, Chinese Academy of Sciences, Beijing 100190, China*

† Electronic supplementary information (ESI) available. See DOI: 10.1039/c8cy00729b

photoanodes. Recently, Lee *et al.* reported that a more active Fe_2O_3 photoanode could maintain its small feature sizes by hybrid microwave annealing (HMA), and a graphite susceptor was used for efficient microwave absorption.[35]

In this work, a thin FeOOH nanowire precursor on FTO was firstly fabricated through a facile hydrothermal method using $FeCl_3{\cdot}6H_2O$ and Na_2SO_4 as starting materials, which was followed by annealing with the HMA method. Subsequently, a C_3N_4 layer was firstly deposited onto the surface of the nanosheet Fe_2O_3 photoanode by vacuum evaporation of bulk C_3N_4. In order to further enhance the PEC performance of Fe_2O_3/C_3N_4, a p-type CoO_x cocatalyst was further deposited onto its surface by a solvothermal method using $Co(CH_3COO)_2{\cdot}4H_2O$ and ammonium hydroxide as reactants. The details of experiments are shown in the Experimental section of the ESI.† In comparison with the pristine Fe_2O_3 film, the onset potential of the $Fe_2O_3/C_3N_4/CoO_x$ photoanode was negatively shifted by about 0.19 V, and its photocurrent density (1.50 mA cm^{-2} at 1.23 V_{RHE}) was about two-fold higher. The photo-to-hydrogen conversion efficiency and incident photo-to-current conversion efficiency (IPCE) at 385 nm reached 0.17% and 81.7%, respectively.

Results and discussion

The crystal structures of Fe_2O_3 and Fe_2O_3/C_3N_4 were characterized by X-ray diffraction (XRD) as shown in Fig. 1. All the peaks can be indexed to Fe_2O_3 (PDF no. 33-0664) marked with solid triangles and FTO marked with solid circles. There is no peak belonging to C_3N_4 probably due to its tiny amounts. Fig. 2a–d show the scanning electron microscopy (SEM) images of the as-synthesized FeOOH, Fe_2O_3, Fe_2O_3/C_3N_4, and $Fe_2O_3/C_3N_4/CoO_x$. FeOOH exists as nanowires on the FTO substrate with diameters of 18 to 30 nm based on the typical transmission electron microscopy (TEM) results (Fig. S1†). The thickness of the as-synthesized FeOOH is about 470 nm estimated from the inset of Fig. 2a. After the HMA treatment, the FeOOH nanowires converted into Fe_2O_3 nanosheets with thickness in the range of 22 to 35 nm (Fig. 2b). The thickness of the Fe_2O_3 film, composed of Fe_2O_3 nanosheets, is about 300 nm (inset of Fig. 2b). The FeOOH nanowires must recrystallize and grow to larger Fe_2O_3 nanosheets during the HMA treatment due to the obvious morphology change. The morphology further changes after the homogeneous C_3N_4 deposition on the top of Fe_2O_3 (Fig. 2c and S2†). The thickness of nanosheets in Fig. 2c and d becomes about 64 nm, indicating that the thickness of deposited C_3N_4 ranges from ~29 to ~42 nm. These values are much larger than that of the layer deposited from exfoliated bulk C_3N_4.[28,29,31] The TEM image of Fe_2O_3 in Fig. 2e further confirms that the HMA treated FeOOH turns into Fe_2O_3 nanosheets. Fig. 2f shows the high-resolution TEM (HRTEM) image of Fe_2O_3, and the calculated interplanar spacing is about 0.27 nm which is consistent with the value of the (104) plane. Due to the poor stability of C_3N_4 under the high voltage used in the characterization, the TEM and HRTEM results of Fe_2O_3/C_3N_4 and $Fe_2O_3/C_3N_4/CoO_x$ were not shown in this work. The elemental mapping results indicate that the Sn^{4+} from FTO has been successfully doped into the Fe_2O_3 photoanode during HMA treatment (Fig. S3†), which is crucial to improve the PEC performance of the Fe_2O_3 photoanode.[3–5]

Fig. 3 shows the X-ray photoelectron spectroscopy (XPS) spectra of Fe_2O_3, Fe_2O_3/C_3N_4, and $Fe_2O_3/C_3N_4/CoO_x$. The C 1s of Fe_2O_3 is located at 284.6 eV (standard reference carbon) and 288.2 eV ascribed to the C═O,[36] which may come from

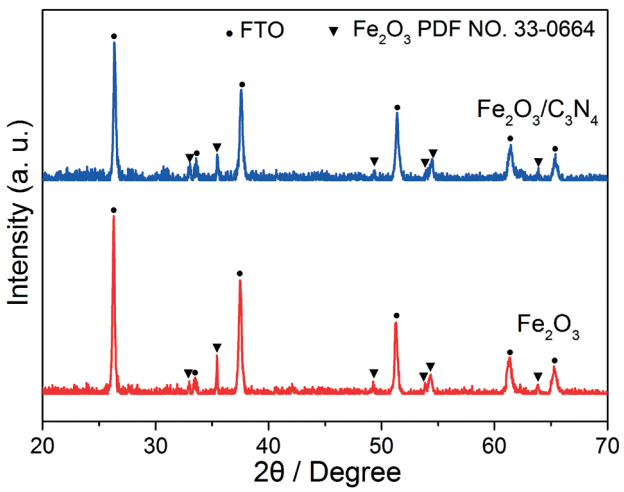

Fig. 1 XRD patterns of Fe_2O_3 and Fe_2O_3/C_3N_4 photoanodes.

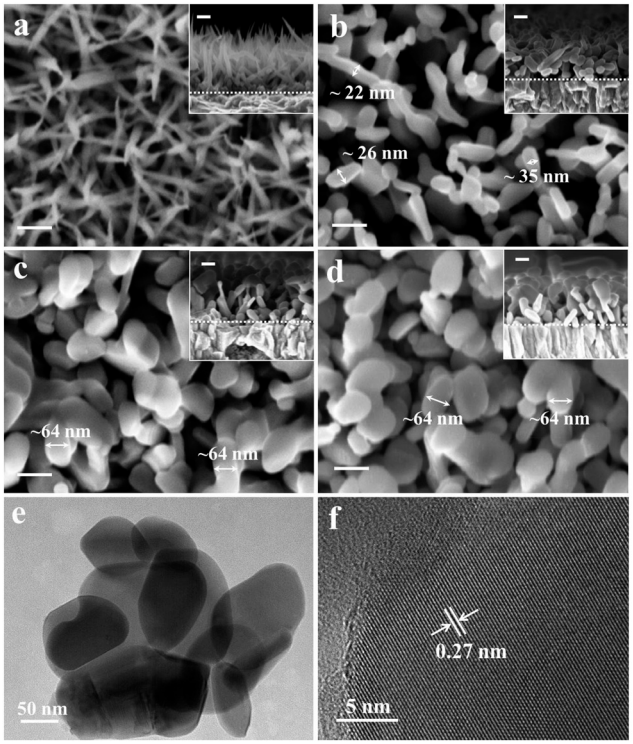

Fig. 2 Typical SEM images of a) FeOOH, b) Fe_2O_3, c) Fe_2O_3/C_3N_4, and d) $Fe_2O_3/C_3N_4/CoO_x$; e) TEM and f) HRTEM images of Fe_2O_3. Scale bars in the picture and inset of a–d: 100 nm.

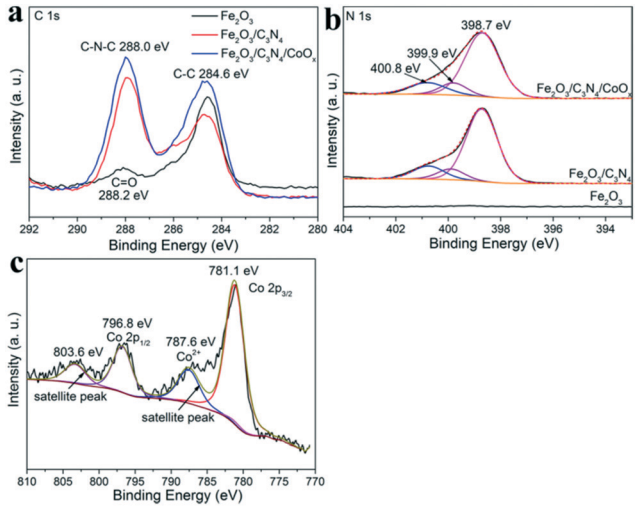

Fig. 3 XPS spectra of a) C 1s, b) N 1s and c) Co 2p of Fe_2O_3, Fe_2O_3/C_3N_4, and $Fe_2O_3/C_3N_4/CoO_x$.

the oxidized C absorbed on the Fe_2O_3 surface during the HMA treatment. The peaks centered at 288.0 eV for Fe_2O_3/C_3N_4 and $Fe_2O_3/C_3N_4/CoO_x$ correspond to the binding energy of C–N–C bonds.[28] There is no signal of N element for pristine Fe_2O_3 as shown in Fig. 3b. However, the high resolution N 1s spectra of Fe_2O_3/C_3N_4 and $Fe_2O_3/C_3N_4/CoO_x$ can be fitted with three Gaussian results at 398.7, 399.9, and 400.8 eV, which correspond to the sp^2-bonded carbon (N–C═N), the tertiary N bonded to carbon atoms as N–$(C)_3$ or H–N–$(C)_2$, and quaternary N bonded to three carbon atoms in the aromatic cycles, respectively.[31] These results indicate that C_3N_4 has been successfully deposited on the surface of Fe_2O_3/C_3N_4 and $Fe_2O_3/C_3N_4/CoO_x$ photoanodes. Fig. 3c shows that there are two obvious peaks centered at 781.1 eV (Co $2p_{3/2}$) and 796.8 eV (Co $2p_{1/2}$), which are consistent with the positions of both Co^{2+} and Co^{3+}, and the satellite peaks at 787.6 eV and 803.6 eV are typical features of Co^{2+},[37] and these findings confirm the existence of CoO_x in the composite.

The PEC performances of the above mentioned photoanodes were characterized in a 1 M NaOH electrolyte (pH = 13.6) under simulated illumination (AM 1.5 G, 100 mW cm^{-2}) at a scan rate of 10 mV s^{-1} (see details in the ESI†). The current density–potential (*J*–*V*) curves are exhibited in Fig. 4a. The dark current densities in all cases are negligible. In Fig. 4a, the photocurrent density of the pristine Fe_2O_3 is about 0.74 mA cm^{-2} at 1.23 V_{RHE}. This value is similar to the results of single Fe_2O_3 photoanodes in many reports.[38–42] However, it is lower than the reported value of the pristine photoanode synthesized by the same HMA method.[35] The reason is likely that the stacked nanosheets (inset in Fig. 2b) in our work are less effective in transporting the photoexcited charges than the vertical nanorods in the reference. When C_3N_4 is deposited on Fe_2O_3, the photocurrent density of water oxidation reaches 1.15 mA cm^{-2} which is about 1.6 times compared with that of the pristine Fe_2O_3. Further CoO_x decoration on Fe_2O_3/C_3N_4 increases the photocurrent density to

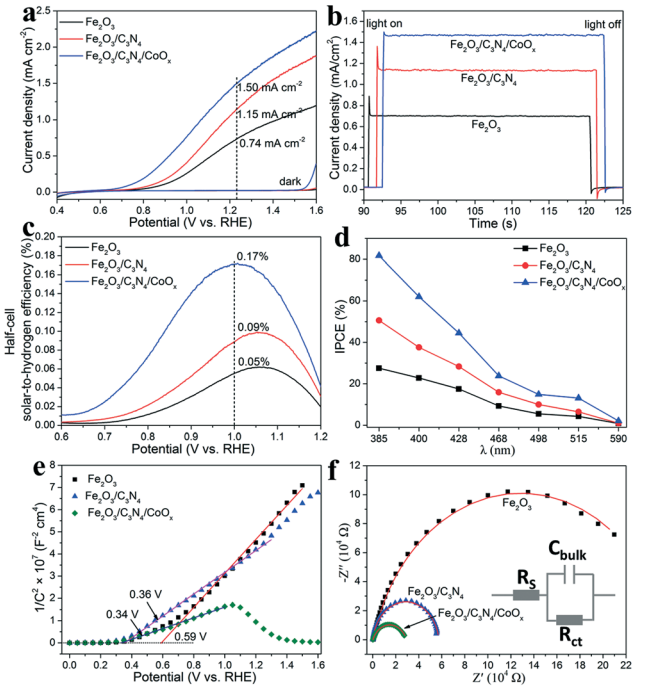

Fig. 4 a) Linear sweep voltammograms and b) stacked transient photocurrent density–potential curves as a function of time of Fe_2O_3, Fe_2O_3/C_3N_4, and $Fe_2O_3/C_3N_4/CoO_x$ photoanodes at 1.23 V_{RHE} under chopped illumination, c) half-cell solar-to-hydrogen efficiency, d) IPCE, e) Mott–Schottky plots, and f) EIS Nyquist plots under illumination of Fe_2O_3, Fe_2O_3/C_3N_4, and $Fe_2O_3/C_3N_4/CoO_x$ photoanodes. Electrolyte: 1 M NaOH (pH = 13.6), light source: AM 1.5 G (100 mW cm^{-2}), scan rate: 10 mV s^{-1}.

1.50 mA cm^{-2} at 1.23 V_{RHE}. The photocurrent onset potential can be defined at the potential when the value of d*J*/d*V* is 0.2 mA cm^{-2} V^{-1}.[43,44] As shown in Fig. S4,† the photocurrent onset potentials shift in the cathodic direction by 0.09 and 0.19 V for Fe_2O_3/C_3N_4 and $Fe_2O_3/C_3N_4/CoO_x$ photoanodes compared with that of Fe_2O_3 (0.81 V_{RHE}), respectively. As a comparison, CoO_x was also used to decorate the pristine Fe_2O_3, and the *J*–*V* curves are exhibited in Fig. S5.† The photocurrent density is about 0.89 mA cm^{-2} at 1.23 V_{RHE}, which is between the values of pristine Fe_2O_3 and Fe_2O_3/C_3N_4. However, the photocurrent onset potential of Fe_2O_3/CoO_x is similar to that of the $Fe_2O_3/C_3N_4/CoO_x$ photoanode. It can be concluded that both C_3N_4 and CoO_x play significant roles in improving the PEC performance of the hybrid photoanode. To evaluate the PEC stability of the photoanodes, long-term characterization was performed at 1.23 V_{RHE} under simulated sun light illumination (Fig. S6†). Fe_2O_3/C_3N_4 and $Fe_2O_3/C_3N_4/CoO_x$ photoanodes show stable PEC performance even after 5 h illumination. In contrast, the photocurrent density of the Fe_2O_3 photoanode decreased by 0.13 mA cm^{-2} and remained stable at about 0.61 mA cm^{-2} after 10 min. This result probably was caused by the higher stability of C_3N_4 in the concentrated alkali electrolyte.

The transient *J*–*V* curves of Fe_2O_3, Fe_2O_3/C_3N_4, and $Fe_2O_3/C_3N_4/CoO_x$ are exhibited in Fig. S7,† which were irradiated under chopped illumination at 1.23 V_{RHE}. The photocurrents

of these samples are consistent with the values at 1.23 V_{RHE} in Fig. 4a. The typical stacked photocurrents of light on and off parts are shown in Fig. 4b. When Fe_2O_3 and Fe_2O_3/C_3N_4 photoanodes are irradiated by light, photogenerated holes transfer to the surface of photoanodes and accumulate due to the slow oxygen evolution reaction (OER) kinetics, or photoexcited carriers oxidize trap states in the bulk and on the surface. These processes result in the anodic current spike.[16] When the light is turned off, electrons flow back from the external circuit and recombine with the accumulated holes on the surface, thus the cathodic transient peak is observed.[16] In our work, the Fe_2O_3/C_3N_4 photoanode shows stronger anodic and cathodic current spikes than Fe_2O_3 as shown in Fig. 4b. The Fe_2O_3/C_3N_4 photoanode exhibits quicker OER kinetics than the Fe_2O_3 photoanode by judging from the photocurrent onset potential (Fig. S4†). Accordingly, the stronger anodic and cathodic current spikes of Fe_2O_3/C_3N_4 must result from the more defects in the evaporated C_3N_4, which can also be proved by the stronger photoluminescence intensity of C_3N_4-decorated Fe_2O_3 than that of the pristine Fe_2O_3 (Fig. 5). When CoO_x was deposited on Fe_2O_3/C_3N_4, both anodic and cathodic current spikes decreased intensively. The CoO_x decoration must passivate the defects on the surface of Fe_2O_3 and Fe_2O_3/C_3N_4 photoanodes (Fig. 4b and S8†). Furthermore, the p-type CoO_x shows excellent hole-transfer and electron-blocking properties due to its relatively high conduction band edge.[45] These two reasons prevent the recombination of the photoexcited carriers, which are also supported by the decreased PL intensity of the $Fe_2O_3/C_3N_4/CoO_x$ film in comparison with those of the pristine Fe_2O_3 and Fe_2O_3/C_3N_4 as shown in Fig. 5.

The half-cell solar-to-hydrogen conversion efficiency (Fig. 4c) of the photoanodes was calculated based on the data in Fig. 4a using the equation: $\eta = (j_p - j_d)(1.23 - |V|)/I_0$, in which j_p, j_d, V, and I_0 are the photocurrent density, the dark current density, the applied potential, and the power density of incident light, respectively. The j_p values are 0.18, 0.37, and 0.75 mA cm^{-2} at 1.0 V_{RHE} under the simulated sunlight of AM 1.5 G illumination (100 mW cm^{-2}) for Fe_2O_3, Fe_2O_3/C_3N_4, and $Fe_2O_3/C_3N_4/CoO_x$, respectively. Correspondingly, the conversion efficiencies are 0.05%, 0.09%, and 0.17%, respectively. The efficiency enhancement is more than 3-fold after the C_3N_4 and CoO_x decoration on the as-synthesized Fe_2O_3.

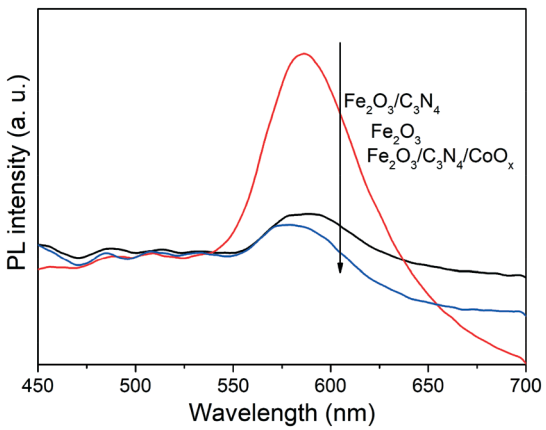

Fig. 5 Photoluminescence (PL) spectra of Fe_2O_3, Fe_2O_3/C_3N_4, and $Fe_2O_3/C_3N_4/CoO_x$ films excited at a laser wavelength of 380 nm.

The IPCE of Fe_2O_3, Fe_2O_3/C_3N_4, and $Fe_2O_3/C_3N_4/CoO_x$ was characterized at 1.23 V_{RHE} using an LED (λ = 385, 400, 428, 468, 498, 515, and 590 nm) as the light source. The tested optical power and photocurrent density are listed in Table S1,† and the IPCE values are shown in Fig. 4d (see calculation details in the ESI†). The trend is $Fe_2O_3/C_3N_4/CoO_x > Fe_2O_3/C_3N_4 > Fe_2O_3$ at each wavelength, and this result agrees well with the PEC activities of these photoanodes in Fig. 4a. The IPCE can reach as high as 81.7% at 385 nm for the $Fe_2O_3/C_3N_4/CoO_x$ photoanode in our work.

According to the above observations, the improved PEC performances strongly depended on the C_3N_4 and CoO_x decoration. Mott–Schottky characterization was carried out to elucidate the reason for activity enhancement with a frequency of 1 kHz in 1 M NaOH. The Fe_2O_3 and Fe_2O_3/C_3N_4 photoanodes exhibit an n-type semiconductor characteristic due to their positive slope as shown in Fig. 4e.[46] However, there is also a negative slope besides a positive one when CoO_x is deposited on Fe_2O_3/C_3N_4, which results from the p-type semiconductor characteristic of CoO_x.[47,48] This further confirms that CoO_x has been successfully decorated on the Fe_2O_3/C_3N_4 photoanode. A similar Mott–Schottky characterization result of the Fe_2O_3/CoO_x photoanode is observed as shown in Fig. S9.† The flatter negative plot means the higher carrier density in the photoanode,[49] and the sequence of the carrier density of these three photoanodes is $Fe_2O_3/C_3N_4/CoO_x > Fe_2O_3/C_3N_4 > Fe_2O_3$. The higher carrier density must originate from the more effective charge separation at the interface of the heterojunction and the much longer lifetime of the photogenerated carriers.[46] Moreover, the flat band potential (V_{fb}) at the semiconductor/electrolyte interface also cathodically shifts. The V_{fb} of the pristine Fe_2O_3 is 0.59 V_{RHE} which is in good agreement with the values in the literature,[50] and the V_{fb} of Fe_2O_3/C_3N_4 and $Fe_2O_3/C_3N_4/CoO_x$ is 0.36 and 0.34 V_{RHE}, respectively. The C_3N_4 modification greatly changes the V_{fb} cathodically shifted by about 0.23 V. This suggests a larger accumulation of electrons in the heterojunction and decreased charge recombination. After the p-type CoO_x decoration, the V_{fb} further cathodically shifts by about 0.02 V for $Fe_2O_3/C_3N_4/CoO_x$, which reflects that the CoO_x can further improve the charge separation.

In order to gain a deep understanding of the charge transfer properties of the photoanodes, the Nyquist plots derived from electrochemical impedance spectroscopy (EIS) measurements were carried out at 0.7 V_{RHE} from 0.01 Hz to 100 kHz under illumination (AM 1.5 G, 100 mW cm^{-2}) as shown in Fig. 4f. The curves were fitted using the model in the inset of Fig. 4f. From the fitting results, the R_{ct} representing the charge transfer resistance of photoexcited holes from the valence band to the electrolyte is calculated to be 255 780, 56 925, and 28 996 Ω for Fe_2O_3, Fe_2O_3/C_3N_4, and $Fe_2O_3/C_3N_4/$

CoO_x, respectively. The decreasing R_{ct} indicates that the interface charge transfer rate has increased after C_3N_4 and CoO_x decoration in sequence. This enhanced charge transfer ability is caused by the reduced accumulation of the charge density at the surface of the photoanodes. This result can also explain why Fe_2O_3/C_3N_4 and $Fe_2O_3/C_3N_4/CoO_x$ photoanodes exhibit higher PEC performance than Fe_2O_3 though there are more defects in C_3N_4.

Fig. 6a shows the UV-vis diffuse reflectance spectra of Fe_2O_3, Fe_2O_3/C_3N_4, $Fe_2O_3/C_3N_4/CoO_x$ films and C_3N_4 powder. The absorption band edge of C_3N_4 powder blue shifts compared with those of the three films. However, the C_3N_4 decoration doesn't shift the absorption band edges of Fe_2O_3/C_3N_4 and $Fe_2O_3/C_3N_4/CoO_x$ films probably due to the tiny amount of the C_3N_4 layer. This result also indicates that the enhanced PEC performances are not caused by the optical properties. Fig. 6b exhibits the band gaps of C_3N_4 and Fe_2O_3 calculated using the following equation:

$$(\alpha h\nu)^{\frac{1}{n}} = A(h\nu - E_g)$$

where A is a material specific constant and the power index n depends on the particular type of optical transition. Here, the values of n are 1/2 and 2 for the direct-band-gap C_3N_4 and indirect-band-gap Fe_2O_3, respectively.[46,51] The calculated values are 2.05 eV for Fe_2O_3 and 2.70 eV for C_3N_4 which agree with the reported ones.[46,51] The absolute position of the charge (pH_{zpc}) can be calculated using the following equation:[52]

$$E^0_{CB} = X - E^e - 1/2E_g$$

Here, X is the absolute electronegativity of the semiconductor, which shows the geometric mean of the absolute electronegativity of the constituent atoms, and is defined as the arithmetic mean of the atomic electron affinity and the first ionization energy; E^e is the energy of free electrons on the hydrogen scale (~4.5 eV); and E_g is the band gap of the semiconductor. The calculated value of X is 5.87 eV for Fe_2O_3. Based on the above equation and the calculated band gap, the conduction band edge (E_{CB}) of Fe_2O_3 (E_g = 2.05 eV) is about 0.35 eV, and the valence band edge (E_{VB}) of Fe_2O_3 is about 2.4 eV. Because C_3N_4 is a polymeric semiconductor, the notation "C_3N_4" is used to describe this class of materials rather than the idealized structure,[53] thus the above equation is not appropriate for the band edge calculation of C_3N_4. According to a previous report, the band positions are E_{CB} = −1.13 eV and E_{VB} = 1.57 eV for C_3N_4.[28]

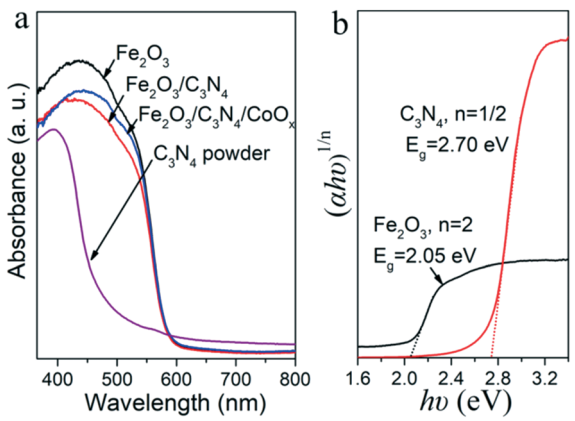

Fig. 6 a) UV-vis diffuse reflectance spectra of Fe_2O_3, Fe_2O_3/C_3N_4, and $Fe_2O_3/C_3N_4/CoO_x$ films and C_3N_4 powder, and b) $(\alpha h\nu)^{1/n}$–$h\nu$ plots of Fe_2O_3 and C_3N_4.

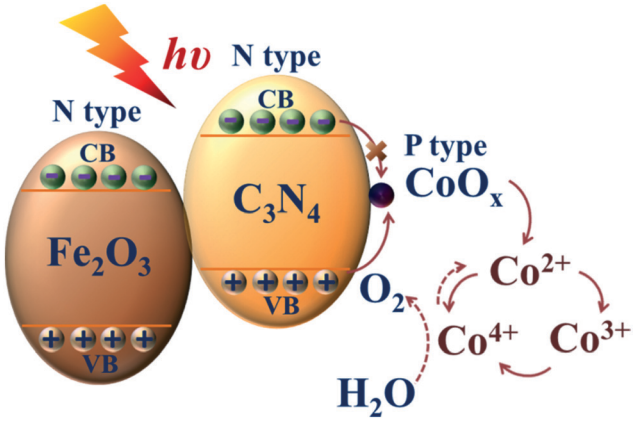

Scheme 1 Proposed mechanism of photoelectrochemical water oxidation over the $Fe_2O_3/C_3N_4/CoO_x$ hybrid photoanode.

Based on the above results, the photoexcited electrons of the C_3N_4 decoration transfer to Fe_2O_3, and favorably move to the Pt counter electrode for H_2 evolution through the FTO substrate. Meanwhile, the holes from Fe_2O_3 migrate toward the surface of C_3N_4 due to the different band potentials. This process improves the charge separation ability across the heterojunction (Fig. 4e). Furthermore, CoO_x particles also effectively suppress the recombination of photogenerated carriers due to the passivation of surface trapped charges (Fig. 4b).[47] Simultaneously, the p-type CoO_x can effectively transfer the photoexcited holes and block the electrons.[45] The stored holes oxidize the CoO_x cocatalyst from Co^{2+} to Co^{3+}/Co^{4+} and finally to Co^{4+}–O intermediates to produce O_2,[28,29] and it needs lower overpotential for PEC water oxidation.[34] After the water oxidation, Co^{4+} was reduced to Co^{2+} that then went into the next catalysis reaction cycle. The proposed mechanism of PEC water oxidation is shown in Scheme 1.

Conclusions

In summary, we have firstly developed a vacuum evaporation strategy to fabricate a C_3N_4-decorated Fe_2O_3 photoanode with efficient PEC water splitting. The decoration of the Fe_2O_3/C_3N_4 photoanode with p-type CoO_x further improved its PEC performance. The resulting hybrid photoanode exhibited greatly enhanced PEC performance. The photocurrent density of the hybrid photoanode was 2-fold as high as that of the

pristine Fe_2O_3 at 1.23 V_{RHE}, and the photocurrent onset potential was cathodically shifted by about 0.19 V. The efficient charge separation, recombination center reduction, and fast charge transfer at the semiconductor/electrolyte interface resulting from C_3N_4 and the p-type CoO_x cocatalyst contribute to the efficient PEC performance for water oxidation. This work provided a novel method to synthesize efficient photoanodes which could be used in other research studies.

Conflicts of interest

There are no conflicts to declare.

Acknowledgements

The research was financially supported by the Shenzhen Science and Technology Research Grant (No. JCYJ20151015162256516, JCYJ20160226105838578), the International Cooperation Project of Shenzhen Science and Technology Research and Development Funds (No. GJHZ20160229122304608), and the Shenzhen Peacock Plan (KQTD2014062714543296).

Notes and references

1 K. Sivula, F. Le Formal and M. Grätzel, *ChemSusChem*, 2011, **4**, 432–449.
2 A. G. Tamirat, J. Rick, A. A. Dubale, W.-N. Su and B.-J. Hwang, *Nanoscale Horiz.*, 2016, **1**, 243–267.
3 Y. Ling, G. Wang, D. A. Wheeler, J. Z. Zhang and Y. Li, *Nano Lett.*, 2011, **11**, 2119–2125.
4 M. Li, Y. Yang, Y. Ling, W. Qiu, F. Wang, T. Liu, Y. Song, X. Liu, P. Fang, Y. Tong and Y. Li, *Nano Lett.*, 2017, **17**, 2490–2495.
5 K. Sivula, R. Zboril, F. Le Formal, R. Robert, A. Weidenkaff, J. Tucek, J. Frydrych and M. Grätzel, *J. Am. Chem. Soc.*, 2010, **132**, 7436–7444.
6 I. S. Cho, H. S. Han, M. Logar, J. Park and X. Zheng, *Adv. Energy Mater.*, 2016, **6**, 1501840.
7 Z. Luo, T. Wang, J. Zhang, C. Li, H. Li and J. Gong, *Angew. Chem., Int. Ed.*, 2017, **56**, 12878–12882.
8 Y. Fu, C. Dong, Z. Zhou, W. Lee, J. Chen, P. Guo, L. Zhao and S. Shen, *Phys. Chem. Chem. Phys.*, 2016, **18**, 3846–3853.
9 J. Liu, C. Liang, G. Xu, Z. Tain, G. Shao and L. Zhang, *Nano Energy*, 2013, **2**, 328–336.
10 Gurudayal, S. Y. Chiam, M. H. Kumar, P. S. Bassi, H. L. Seng, J. Barber and L. H. Wong, *ACS Appl. Mater. Interfaces*, 2014, **6**, 5852–5859.
11 J. Y. Kim, G. Magesh, D. H. Youn, J. Jang, J. Kubota, K. Domen and J. S. Lee, *Sci. Rep.*, 2013, **3**, 2681.
12 Y. Hu, A. Kleiman-Shwarsctein, A. J. Forman, D. Hazen, J. Park, E. W. Mcfarland, S. Barbara and S. Barbara, *Chem. Mater.*, 2008, **20**, 3803–3805.
13 I. Cesar, A. Kay, J. A. G. Martinez and M. Gra, *J. Am. Chem. Soc.*, 2006, **128**, 4582–4583.
14 Y. Zhang, S. Jiang, W. Song, P. Zhou, H. Ji, W. Ma, W. Hao, C. Chen and J. Zhao, *Energy Environ. Sci.*, 2015, **8**, 1231–1236.
15 R. Franking, L. Li, M. A. Lukowski, F. Meng, Y. Tan, R. J. Hamers and S. Jin, *Energy Environ. Sci.*, 2013, **6**, 500–512.
16 C. Li, T. Wang, Z. Luo, S. Liu and J. Gong, *Small*, 2016, **12**, 3415–3422.
17 P. S. Bassi, R. P. Antony, P. P. Boix, Y. Fang, J. Barber and L. H. Wong, *Nano Energy*, 2016, **22**, 310–318.
18 J. Deng, X. Lv, K. Nie, X. Lv, X. Sun and J. Zhong, *ACS Catal.*, 2017, **7**, 4062–4069.
19 F. Boudoire, R. Toth, J. Heier, A. Braun and E. C. Constable, *Energy Environ. Sci.*, 2014, **7**, 2680–2688.
20 Z. Luo, C. Li, D. Zhang, T. Wang and J. Gong, *Chem. Commun.*, 2016, **52**, 9013–9015.
21 M. G. Ahmed, T. A. Kandiel, A. Y. Ahmed, I. Kretschmer, F. Rashwan and D. Bahnemann, *J. Phys. Chem. C*, 2015, **119**, 5864–5871.
22 Y. Hou, F. Zuo, A. Dagg and P. Feng, *Angew. Chem., Int. Ed.*, 2013, **52**, 1248–1252.
23 W. Che, W. Cheng, T. Yao, F. Tang, W. Liu, H. Su, Y. Huang, Q. Liu, J. Liu, F. Hu, Z. Pan, Z. Sun and S. Wei, *J. Am. Chem. Soc.*, 2017, **139**, 3021–3026.
24 G. Liu, T. Wang, H. Zhang, X. Meng, D. Hao, K. Chang, P. Li, T. Kako and J. Ye, *Angew. Chem., Int. Ed.*, 2015, **54**, 13561–13565.
25 X. Wang, K. Maeda, A. Thomas, K. Takanabe, G. Xin, J. M. Carlsson, K. Domen and M. Antonietti, *Nat. Mater.*, 2009, **8**, 76–80.
26 Y. Liu, Y. X. Yu and W. De Zhang, *Int. J. Hydrogen Energy*, 2014, **39**, 9105–9113.
27 Y. Liu, F. Y. Su, Y. X. Yu and W. De Zhang, *Int. J. Hydrogen Energy*, 2016, **41**, 7270–7279.
28 J. Hou, H. Cheng, O. Takeda and H. Zhu, *Energy Environ. Sci.*, 2015, **8**, 1348–1357.
29 Y. Hou, F. Zuo, A. P. Dagg, J. Liu and P. Feng, *Adv. Mater.*, 2014, **26**, 5043–5049.
30 C. Cheng, J. Shi, Y. Hu and L. Guo, *Nanotechnology*, 2017, **28**, 164002.
31 C. Feng, Z. Wang, Y. Ma, Y. Zhang, L. Wang and Y. Bi, *Appl. Catal., B*, 2017, **205**, 19–23.
32 M. Barroso, C. A. Mesa, S. R. Pendlebury, A. J. Cowan, T. Hisatomi and K. Sivula, *Proc. Natl. Acad. Sci. U. S. A.*, 2012, **109**, 15640–15645.
33 J. Guan, C. Ding, R. Chen, B. Huang, X. Zhang, F. Fan, F. Zhang and C. Li, *Chem. Sci.*, 2017, 6111–6116.
34 X. Chang, T. Wang, P. Zhang, J. Zhang, A. Li and J. Gong, *J. Am. Chem. Soc.*, 2015, **137**, 8356–8359.
35 J. Y. Kim, D. H. Youn, J. H. Kim, H. G. Kim and J. S. Lee, *ACS Appl. Mater. Interfaces*, 2015, **7**, 14123–14129.
36 R. Madhuvilakku, S. Alagar, R. Mariappan and S. Piraman, *Sens. Actuators, B*, 2017, **253**, 879–892.
37 F. Zhang, A. Yamakata, K. Maeda, Y. Moriya, T. Takata, J. Kubota, K. Teshima, S. Oishi and K. Domen, *J. Am. Chem. Soc.*, 2012, **134**, 8348–8351.
38 J. Y. Kim, J. W. Jang, D. H. Youn, G. Magesh and J. S. Lee, *Adv. Energy Mater.*, 2014, **4**, 1400476.
39 O. Zandi and T. W. Hamann, *J. Phys. Chem. Lett.*, 2014, **5**, 1522–1526.

40 P. Zhang, T. Wang, X. Chang, L. Zhang and J. Gong, *Angew. Chem., Int. Ed.*, 2016, **55**, 5851–5855.
41 L. Xi, P. D. Tran, S. Y. Chiam, P. S. Bassi, W. F. Mak, H. K. Mulmudi, S. K. Batabyal, J. Barber, J. S. C. Loo and L. H. Wong, *J. Phys. Chem. C*, 2012, **116**, 13884–13889.
42 M. Barroso, A. J. Cowan, S. R. Pendlebury, M. Grätzel, D. R. Klug and J. R. Durrant, *J. Am. Chem. Soc.*, 2011, **133**, 14868–14871.
43 F. Le Formal, M. Grätzel and K. Sivula, *Adv. Funct. Mater.*, 2010, **20**, 1099–1107.
44 C. Du, X. Yang, M. T. Mayer, H. Hoyt, J. Xie, G. McMahon, G. Bischoping and D. Wang, *Angew. Chem., Int. Ed.*, 2013, **52**, 12692–12695.
45 E. Nurlaela, H. Wang, T. Shinagawa, S. Flanagan, S. Ould-Chikh, M. Qureshi, Z. Mics, P. Sautet, T. Le Bahers, E. Cánovas, M. Bonn and K. Takanabe, *ACS Catal.*, 2016, **6**, 4117–4126.
46 F. Zhan, R. Xie, W. Li, J. Li, Y. Yang, Y. Li and Q. Chen, *RSC Adv.*, 2015, **5**, 69753–69760.
47 M. Zhong, T. Hisatomi, Y. Kuang, J. Zhao, M. Liu, A. Iwase, Q. Jia, H. Nishiyama, T. Minegishi, M. Nakabayashi, N. Shibata, R. Niishiro, C. Katayama, H. Shibano, M. Katayama, A. Kudo, T. Yamada and K. Domen, *J. Am. Chem. Soc.*, 2015, **137**, 5053–5060.
48 K. Nagashima, T. Yanagida, M. Kanai, U. Celano, S. Rahong, G. Meng, F. Zhuge, Y. He, B. Ho Park and T. Kawai, *Appl. Phys. Lett.*, 2013, **103**, 173506.
49 J. Liu, Y. Y. Cai, Z. F. Tian, G. S. Ruan, Y. X. Ye, C. H. Liang and G. S. Shao, *Nano Energy*, 2014, **9**, 282–290.
50 P. Dias, A. Vilanova, T. Lopes, L. Andrade and A. Mendes, *Nano Energy*, 2016, **23**, 70–79.
51 S. Shen, S. A. Lindley, X. Chen and J. Z. Zhang, *Energy Environ. Sci.*, 2016, **9**, 2744–2775.
52 Z. Mei, M. Zhang, J. Schneider, W. Wang, N. Zhang, Y. Su, B. Chen, S. Wang, A. L. Rogach and F. Pan, *Catal. Sci. Technol.*, 2017, **7**, 982–987.
53 J. Zhang, X. Chen, K. Takanabe, K. Maeda, K. Domen, J. D. Epping, X. Fu, M. Antonieta and X. Wang, *Angew. Chem., Int. Ed.*, 2010, **49**, 441–444.

